HHS Public Access

Author manuscript

Anal Chem. Author manuscript; available in PMC 2016 March 22.

Published in final edited form as:

Anal Chem. 2011 February 15; 83(4): 1207–1213. doi:10.1021/ac1030607.

Compositional Mapping of the Surface and Interior of Mammalian Cells at Submicrometer Resolution

Christopher Szakal[*,†], **Kedar Narayan**[‡], **Jing Fu**[‡], **Jonathan Lefman**[†], and **Sriram Subramaniam**[‡]

[†]Surface and Microanalysis Science Division, National Institute of Standards and Technology, 100 Bureau Drive, Gaithersburg, Maryland 20899-8371, United States

[‡]Laboratory of Cell Biology, Center for Cancer Research, National Cancer Institute, National Institutes of Health, Bethesda, Maryland 20892, United States

Abstract

We present progress toward imaging of chemical species within intact mammalian cells using secondary ion mass spectrometry, including the simultaneous mapping of subcellular elemental and molecular species along with intrinsic membrane-specific cellular markers. Results from imaging both the cell surface and cell interior exposed by site-specific focused ion beam milling demonstrate that in-plane resolutions of approximately 400–500 nm can be achieved. The results from mapping cell surface phosphatidylcholine and several other molecular ions present in the cells establish that spatially resolved chemical signatures of individual cells can be derived from novel multivariate analysis and classification of the molecular images obtained at different *m/z* ratios. The methods we present here for specimen preparation and chemical imaging of cell interiors provide the foundation for obtaining 3D molecular maps of unstained mammalian cells, with particular relevance for probing the subcellular distributions of small molecules, such as drugs and metabolites.

Introduction

Knowledge of the spatial distributions of proteins, metabolites, and elements within cells is potentially important for understanding cytochemical function in health and disease. Submicrometer resolution is required for localizing subcellular regions of interest, and techniques based on optical technology, such as fluorescence microscopy, have proven to be very useful for monitoring discrete chemical changes within and around cells. However, fluorescence imaging is usually restricted to imaging natively fluorescent molecules or those that have been specifically attached to analytes of interest. In contrast, mass spectrometry-based techniques provide unique opportunities for achieving simultaneous detection of multiple, unlabeled cellular components. Matrix-assisted laser desorption ionization mass spectrometry (MALDI-MS) has been used extensively for tissue imaging, although the typical spatial resolutions achieved (around 20–50 μm) make it unsuitable for subcellular imaging of most mammalian cells. Secondary ion mass spectrometry (SIMS)-based

[*]Phone: (301) 975-3816. Fax: (301) 417-1321. cszakal@nist.gov.

approaches, with SIMS primary ion beams as small as 50–500 nm, are capable of much higher resolution and are therefore useful for single cell chemical imaging mass spectrometry. Significant progress has already been made in this area, and SIMS imaging of single cells has been reported for a variety of elemental and isotopic species,(1–16) for high-concentration lipids and/or cholesterol,(16–32) and for lipids with corresponding salt distributions.(16, 33–38) As an example of a biologically relevant work, Ostrowski and co-workers have reported that low-curvature lipids such as phosphatidylcholine were suppressed at mating junctions of *Tetrahymena* cell pairs in favor of more highly curved lipids such as phosphatidylethanolamine.(19)

Despite these advances, SIMS imaging continues to yield few biological discoveries and only modest success with subcellular molecular imaging because of several shortcomings such as smaller mass ranges compared to MALDI-MS (typically less than 500 *m/z* for SIMS), higher primary beam-induced molecular damage levels, and generally low molecular ionization probabilities of target molecules. Furthermore, there have also been challenges in developing sample preparation/preservation protocols that maintain the chemical integrity of the cells, minimizing molecular damage from the incident beam that limits the ability to generate three-dimensional data sets, and achieving the theoretical spatial resolution limits. Here, we present advances both in specimen preparation and in strategies to extend the imaging into the third dimension by combining SIMS with focused ion beam (FIB) milling. These methods provide new opportunities for the direct imaging and localization of drug molecules, metabolites, organelle-specific tags, and chemical signatures within the cell while allowing for the acquisition of molecular maps at different cell depths. We additionally provide preliminary results for an alternative multivariate analysis methodology meant specifically for differentiating between ion-specific images. This work presents a comprehensive approach to accomplish the aim of single cell mass spectrometric imaging and will be utilized in future studies of specific molecular targets within cells.

Experimental Section

Overall Experimental Scheme

The general principle of single cell secondary ion mass spectrometry (SIMS) imaging and its combination with a Ga^+ focused ion beam (FIB) is illustrated in Figure 1. The FIB is used to mill flash-frozen, freeze-dried HeLa cells in a plane parallel to the surface (with the milling path marked by a dotted line). The resulting exposed cellular interiors are interrogated by SIMS, where material is desorbed from each targeted pixel area such that characteristic elemental and molecular ions of the appropriate polarity are mass-analyzed en route to a microchannel plate detector. The full mass spectrum from *m/z* 0 to 1000 is detected in parallel for each pixel. Maps of the pixels indicative of where individual chemical species of interest emanate are generated. The maps are subsequently subjected to a newly developed computational algorithm aimed at identifying distinct cellular and subcellular molecular localizations. Overlays of these localizations produce detailed molecular maps of molecular chemistries within and around single cells.

Cell Growth

Silicon substrates were cut with a diamond scribe from 5 mm × 5 mm prediced squares (Virginia Semiconductor, Fredericksburg, VA) into approximately 2 mm × 2 mm pieces, and were sterilized for purposes of cell culture by careful rinsing in ethanol and HPLC-grade water. All preparations were performed in a process free of contamination from poly(dimethyl)siloxane (PDMS), (a common surface contaminant in SIMS analysis), by refraining from the use of solvents and cell growth conditions that could allow contact with certain plastics. The silicon pieces were placed in a 96-well plate, and HeLa cells were seeded into the wells at a cell density of approximately 1000 cells/well after overnight growth in Roswell Park Memorial Institute (RPMI) phosphate buffered saline (PBS) containing 10% fetal bovine serum (FBS).

Cell Preparation for Mass Spectrometry

A detailed rationale for the approach used to prepare the cells for imaging mass spectrometry in this work will not be discussed here as many of the concepts have been discussed recently.(38) Silicon chips with adherent cells grown as above were washed in 5 mL of phosphate-buffered saline (PBS) and 1% bovine serum albumin (BSA) at 37 °C for 5 min and then maintained at 37 °C for 5–10 min, blotted with Whatman no. 1 filter paper (Whatman, Inc., Piscataway, NJ) (Certain commercial equipment, instruments, or materials are identified to adequately specify the experimental procedure. Such identification does not imply recommendation or endorsement of the National Institute of Standards and Technology, nor does it imply that the materials or equipment identified are necessarily the best available for the purpose.) for 2 s, and plunge-frozen in liquid ethane (temperature of approximately −180 °C) cooled by liquid nitrogen. The frozen silicon pieces were transferred to liquid nitrogen for storage until they were mounted on a liquid nitrogen-cooled stage for lyophilization (freeze-drying). Lyophilization was performed slowly such that the cells were maintained at liquid nitrogen temperatures for 5 h before warming to room temperature over a period of 10 h. The silicon pieces were then gently rinsed in a small volume of HPLC-grade water for 5 s, and excess water was wicked away by gentle contact with a dry piece of filter paper. This final step removes the majority of salt contamination on the silicon chip while maintaining the integrity of the internal cellular structures. The salt removal from the cell surfaces was confirmed in the ion-specific images.

Focused Ion Beam (FIB) Milling

FIB milling on flash-frozen, freeze-dried HeLa cells was performed prior to mass spectrometric imaging. The silicon pieces with prepared cells were mechanically fixed on a pretilted sample holder and mounted in a Nova 200 FIB/scanning electron microscope (SEM) instrument (FEI, Hillsboro, Oregon) equipped with a gallium liquid metal ion source. Both sample alignment and milling processes were monitored with 2–3 keV SEM imaging, and a specified grazing incidence angle (90° ± 0.5° to 1.0° from the surface normal) between the silicon piece and ion beam direction was achieved by tilting the sample stage. A beam of 30 keV gallium ions was used to mill the targeted cells, with ion currents at approximately 100 pA. The corresponding beam diameter (fwhm) was approximately 23 nm, and beam scanning was controlled by pattern generation with the instrument software interface.

Secondary Ion Mass Spectrometry (SIMS)

FIB-milled cells are transferred from the FIB instrument to the SIMS instrument through ambient air via a container free of PDMS. The quick exposure to room air is likely a benefit to the SIMS analysis of the FIB-milled cells by allowing for adsorbed proton-containing species to aid in molecular ionization. The prepared cells on silicon pieces were mounted to the top of a SIMS stage with carbon tape such that no carbon tape was visible when viewed from above. An IonToF IV secondary ion mass spectrometer (IonTof USA, Inc., Chestnut Ridge, NY) equipped with 25 keV Bi_n^+ and 10 keV SF_5^+ ion source columns was used for the single cell imaging at vacuum pressures in the 10^{-6} Pa (10^{-8} Torr) range. Since the mass analyzer is of the time-of-flight variety, all desorbed ions from *m/z* 0 to 1000 were detected in parallel. Briefly, each image was acquired by focusing Bi_3^+ primary ions at 25 keV (less than 0.01 pA of pulsed current) in the “burst alignment” mode at a 10 kHz pulse rate and 120–130 ns pulse widths. Primary ions were digitally rastered into (256 × 256) pixel images at raster sizes indicated in each figure. Each pixel area was sampled by applying 50–200 primary ion beam pulses, with the counts of each mass summed over the duration of data acquisition for each respective pixel.

Image Data Analysis

Data sets are structured as multispectral 2D images. Each pixel contains a spectrum defined by intensity values corresponding to particular masses. Both manual and automated analyses of mass spectrometric images were conducted. Manual analysis was performed by first visually identifying ion-specific images that have nonuniform intensity distributions. Attempts were made to classify these images based on morphological similarities or colocalization patterns of common pixel intensities. Images of individual masses or classes of colocalized masses were combined using a two-color or three-color (RGB) display with postacquisition analysis tools provided by the instrument manufacturer. This arduous approach required several days of visual inspection-based manual image analysis and did not reveal all relevant areas of colocalization within the cell volumes. As an alternative, computational algorithms can be helpful in mining through the hundreds of ion-specific maps for each cell set so that molecular localizations can be identified more objectively and with higher-throughput.

Automated classification of the mass groups was achieved using an algorithm developed specifically for this project. The algorithm makes use of the *k*-means clustering method and is implemented via in-house code in the scientific computing software MATLAB (The MathWorks, Inc., Natick, MA). Ion-specific images of spectral peaks above baseline intensity are read from the instrument software-generated binary files to generate a raw image stack. A mask can be made with the instrument software to designate only pixels of interest (which in this case were those pixels where cells were present in the images, as displayed in Figure 4a,b). The image stack is multiplied by the mask so that noncell-based pixels have a value of zero and contribute less to the *k*-means calculation. Data are subjected to the *k*-means method by incrementing the starting *k*-value until the algorithm outputs a similar number of member images in each class over many subsequent iterations. Specifically, for each increment, the starting centroids were determined by performing *k*-means on a randomly selected 10% of the data set before iterating the calculation five times

using these starting centroids to ensure that a local minimum is found. Each image is correlated to all of the calculated centroids, and all images are separated into classes based on the centroid to which they have the highest correlation. These image classes can then be combined in RGB- or lookup table-based overlays like the manual image analysis provided but can now do so with a more robust statistical support for such image class claims. Additional details of the novel automated algorithms will be presented in a subsequent manuscript, at which time the code will be made publicly available.

For the panels a and b in Figure 4, the most highly correlating images in each *k*-means generated class are summed and renormalized to the 0–255 8-bit pixel intensity scale using the open source image data program Fiji, with further details in the Figure 4 caption. The panel images are displayed as color pixel intensity threshold maps, where the ion-specific image data is not subjected to any changes in image brightness or contrast. Instead, image pixels of a certain pixel intensity range are assigned a color so that small variations in the most importantly differentiating pixel intensity ranges are more easily visualized. This threshold approach was accomplished using the public domain image processing program Lispix, with additional details of the threshold procedure outlined elsewhere.(39)

Results and Discussion

The images in Figure 2 depict time-of-flight (TOF)-SIMS compositional maps of several individual unstained HeLa cells following plunge-freezing in liquid ethane and lyophilization to remove vitrified water. Both the total ion image (i.e., sum of all elemental and molecular ion intensities obtained in each pixel) and an overlay of the phosphatidylcholine headgroup (*m/z* 184) from the cell surface and extracellular sodium (*m/z* 23) are shown in parts a and b of Figure 2, respectively. Parts c and d of Figure 2 display the individual ion-specific maps of the sodium and the phosphatidylcholine, respectively. The lipid signal is localized to the contours of each cell, indicative of chemically intact membranes, while more sodium is visible on the substrate than the cell surface. Both observations serve as verification of the sample preparation methods used herein. If the cells had ruptured during cell preparation, lipid signal would be homogeneous across the imaging area and not confined to the cell shapes. Additionally, HeLa cells have filopodia with widths of approximately 300–400 nm,(40, 41) which can be visualized in all images but are especially visible in the total ion image (Figure 2a) and the overlay inset (Figure 2b). The ability to visualize these features verifies the submicrometer resolution of the methodology. Alternatively, a zoom of the image shows each streak of lipid signal along the filopodia in Figure 2b to be one pixel wide, with one pixel in that image set being approximately 410 nm (105 μm/256 pixels).

In an effort to go beyond the SIMS-only sputter erosion approach at obtaining chemical mapping information inside of cells in the literature,(16, 24, 27, 31, 35, 37) we developed an alternative method for molecular chemical mapping of cells in three dimensions by supplanting the controlled sputter erosion normally performed within TOF-SIMS with focused ion beam (FIB) milling. (Note that a very recent work used FIB and elemental/isotopic SIMS methodologies for a cell imaging project(14) but was limited in its utility because of not being able to map multiple known and unknown molecular signatures). The

gallium ion beam can be used to section the cell at a chosen depth, followed by high-resolution SIMS imaging. The iterative process between FIB milling and SIMS imaging represents an important distinction regarding this approach compared with that mentioned in the literature. The conventional approach of dual-beam SIMS depth profiling utilizes a larger cluster ion beam to erode material and a smaller, more focused ion beam to image the resulting surface. The issue related to cell depth profiling is that the imaging beam can create its own damage accumulation in the cellular material to the point where that damage can no longer be removed by the sputter beam.(42, 43) This reduces depth resolution considerably and can even prevent a full 3D image set from being acquired, although some of the most recent discussions in SIMS depth profiling have focused on potential new directions for reducing this problem.(44–46) In order to create 3D data sets in this work, the depth resolution can be maintained throughout the cell depth by removing any SIMS analysis beam-induced damage with the FIB milling. Consequently, the ultimate depth resolution will depend not on the SIMS conditions but on the FIB parameters, which we estimate based on milling performed to date to be between 20 and 40 nm. Compared with altered layer thickness values of trimeric high-energy primary cluster ions reported elsewhere,(47) the analysis beam damage can extend beyond 20 nm into soft targets such as cells. With the use of controlled FIB milling, a thin section of sample can be removed of a size comparable to the analysis beam-induced damage thickness to expose a fresh undamaged slice for analysis. This procedure allows for all residual damage due to the SIMS analysis beam to be removed within this depth, whereas in a SIMS-only depth profiling approach, the residual damage can accumulate throughout the cell erosion depth, despite the best efforts of a cluster ion beam to remove such damage. An additional advantage to this approach, compared to other FIB approaches, involves the grazing incidence of the FIB milling. Rather than milling the cells vertically and creating a sidewall, in this work we used a FIB milling angle of ±0.5–1° from the cell surface; thus, any residual surface damage from FIB gallium ions is relatively minimal, potentially allowing for molecular ions to still be detected in the SIMS imaging analysis. With this shallow milling angle, damage from the FIB is theoretically minimized to only the extension of the lateral component tail of the gallium beam shape or on the order of a couple of nanometers. Even if that small amount of gallium into the remaining sample did cause a problem by minimizing molecule detection, a limited fluence of cluster primary ions could possibly be used to remove that small amount of FIB-induced milling damage. We are not convinced that such cluster ion sputtering is either required or particularly helpful for subsequent high-resolution SIMS imaging since we have not identified such damage from the FIB while utilizing the approach described in this work. Ultralow energy FIB milling conditions, with Ga^+ ions between 2 and 5 keV, should by conventional wisdom reduce the lateral beam-induced cell damage and hence provide the best conditions for subsequent SIMS imaging. However, we find that such low FIB energies do not produce enough sputtering yield to actually mill across the entire cell and instead can create visible tracks or “curtains”(48) into soft materials such as these, resulting in rougher milled surfaces than the higher energies. We are currently experimenting with intermediate energies to find the optimum relationship between FIB milling rate and molecular damage reduction.

Separate clusters of cells were identified from the SEM images and sectioned by the FIB to reveal their interiors as noted above, with results shown in Figure 3. In one set (left panels), we milled only one of the cells, leaving two control cells untouched, while in the other set (right panels), all three cells were at least partially sectioned by a wider sweep of the focused ion beam. Since the FIB milling is parallel with the surface to remove only the tops of the respective cells (depicted in parts a and b of Figure 4 with orange dashed lines), a visible change in cell shape is not observed when viewed from above. The images in Figure 3a,b display the SEM secondary electron images from these two cell clusters, showing morphological electron micrographs of the cell sections. Individual panels in parts c–f of Figure 3 represent the positive polarity ion-specific images of two of the many peaks detected for these cells; the phosphatidylcholine headgroup ion at *m/z* 184 is displayed in Figure 3c,d, and an unassigned yet prevalent signal at *m/z* 274 is displayed in Figure 3e,f. Color compositional overlay maps of the two molecular localizations versus background silicon are displayed in Figure 3g,h. FIB milling produces a dramatic change in the shape of the phosphatidylcholine maps: the lipid membrane molecular maps display voids in signal intensity where the membrane area has been milled away by FIB, whereas in the non-FIB-milled control cells, lipid intensity is spread evenly across the entire cell surface visible to the ion beam. Additionally, molecular signals of other species can now be detected at submicrometer resolution inside of the FIB-milled cells. The signals are believed to be molecular because of their behavior under cluster ion sputtering. Whereas several other intensities above *m/z* 150 retain their intensities after SF_5^+ sputtering (implying that they are likely to be inorganic clusters), the *m/z* 274 disappears in intensity in a manner consistent with either molecular damage from the analysis and/or sputter beams or direct material removal of a thin molecular film. Importantly for the single cell imaging approach, the *m/z* 274 signals are more visible in the areas where the cellular interiors have been revealed by FIB milling; thus, our protocol provides for the plausibility of monitoring specific molecular signatures inside cells by mass spectrometric imaging. Also, we note that these cells were not subjected to sputter-cleaning with a cluster ion beam prior to imaging, and yet we still obtained well-resolved chemical distributions detectable immediately after FIB cross-sectioning. (FIB milling of the cells followed by controlled cluster ion beam sputtering and subsequent high-resolution submicrometer compositional mapping is planned for future technique development studies). The color overlays in Figure 3g,h display the molecular maps of the phosphatidylcholine-based lipid headgroup in green, the unassigned *m/z* 274 signals in red, and the silicon substrate background in blue. Here, the distinct shapes of the FIB-milled cells show the boundaries between lipid membrane signals and the cell interiors, illustrating the ability to obtain molecular maps inside of mammalian cells at submicrometer resolution with this method. We can also identify which cells are worthy of detailed SIMS imaging analysis by monitoring the shape of the lipid signal. For example, in the bottom right of Figure 3h, the bottom right cell has clearly ruptured where other cells are intact due to their distinct lipid signal edge with respect to the substrate.

The panels in Figure 3 were generated by the manual image processing approach described earlier. The images in Figure 4 were generated using the *k*-means algorithm as outlined in the Experimental Section. In addition to the speed and objectivity benefits of the automated classification approach, peak assignments of signals such as at *m/z* 274 can potentially be

determined if the algorithm can provide spatially appropriate peaks that colocalize with certain chemical species. The panels in Figure 4a–d represent three distinct classes of ion-specific images obtained using the masked data algorithm approach outlined in the Experimental Section, with the images corresponding to one of the data sets previously shown in Figure 3. One class relates to lipid signatures, where the four highest correlating images within the class were from signals attributed to the phosphatidylcholine headgroup and displayed in Figure 4b as combinations of ions at *m/z* 104, 58, 86, and 184. The highest lipid-based pixel intensities colored in red and yellow arise from the intact control cells as well as the portion of the FIB-milled cells left unperturbed by the ion milling. These results are consistent with the expectation that the lipid signals should be highest where the lipid membrane has not been removed by the focused ion beam. The lowest lipid-based pixel intensities (as defined as the masses 58, 86, 104, and 184) are colored green and violet and arise from the edges of the cells where intensities are expected to diminish because of the difficulty in extracting secondary ions from these highly curved regions. The lowest intensities are also present where the membrane was removed by the FIB milling or where the inside of the cell is exposed. The large amount of violet pixels (lowest intensities) present inside of the milled cell should not be mistaken as small amounts of membrane present but more a visualization of noise level pixels since the scale for violet is for pixel intensities of 1–24. This clarification also exemplifies an additional benefit of this visualization method: not only can the pixel intensity threshold scale be very instructive for observing subtle localization patterns and chemical gradients inside of cells at submicrometer resolution, but the method also obviates the need to denoise the images since background levels can have their own pixel intensity scale/color.

The panel in Figure 4a combines the three highest correlating images to that particular class, which localizes material to species that are highest in intensity inside of the FIB-milled HeLa cells, at *m/z* 69, 274, and 230. Again the pixel intensity threshold approach is used to visualize the summed image class data, revealing the largest pixel intensities (red) originate inside of the cell where the membrane was milled away by the focused ion beam. The yellow and green pixels of intermediate pixel intensities show some of the gradients that these signals present around the perimeter of the highest intensities, and the violet pixels of lowest intensities are inversely proportional in their locations to the highest lipid-based intensities in the top right panel. The *m/z* 69 peak is theoretically a combination of the generic hydrocarbon $C_5H_9^+$, earlier found to be a marker of cellular content,(19) and any residual $^{69}Ga^+$ from the FIB milling. The long pulse widths preclude this analysis from having the mass resolving power necessary to distinguish inorganic and organic species of nominal mass 69. However, the FIB sources used for cell milling are not isotopically pure, meaning that a high abundance of *m/z* 71 should colocalize with the *m/z* 69 inside of the cells if the signal from *m/z* 69 was largely due to lateral gallium implantation/damage. The *m/z* 71 does not localize inside of the cells and in fact produces the fifth highest correlating ion-specific image in the class shown with the lipid ions in Figure 4b. This confirms our expected gallium-induced implantation/damage at the shallow milling angles used here to be minimal, and allows for the assignment of the ion to be the hydrocarbon expected in the cytoplasm of the cell. The other two ions displayed in the inside cell class (*m/z* 274 and 230) are currently unidentified but are interesting because of their higher mass than other species

localizing to the cell interior. We are currently designing experiments to determine the identity of these ions, including the hypothesis of these peaks being cellular metabolites or possibly being indicative of a cellular uptake mechanism from a molecule or molecules exposed to the cells during their growth period.

The background class was produced without using a cell-specific mask but with all other algorithm parameters the same. The panel in Figure 4c combines the images of the four highest correlating images to that colocalization pattern at *m/z* 30, 44, 70, and 72. Note that the sample area was not sputter-cleaned and we believe that at least a couple of the background peaks can be attributed to species made up of silicon and oxygen. The pixel intensity threshold scale reveals the vast majority of high signals come from the background silicon and not the cells, which is to be expected. Using the threshold maps for the other class images of either the membrane or cell interior shows subtleties to the localization patterns that would (1) not be discernible otherwise because of difficulty in visualization and (2) not be visible had the cell-specific mask not been employed. Figure 4d is a simple RGB overlay of the three component classes in parts a, b, and c of Figure 4, with no additional corrections made to the image.

Conclusions

We have presented a method for imaging diverse chemical moieties within intact mammalian cells, including the simultaneous mapping of elemental and molecular species along with intrinsic membrane-specific cellular markers. This method includes appropriate sample preparation protocols to maintain the physical and chemical integrity of treated mammalian cells and well-developed mass spectrometric imaging procedures. Furthermore, our findings provide confidence in being able to detect signals after focused ion beam (FIB) milling from inside of the high-protein background of single mammalian cells. We have demonstrated that submicrometer molecular imaging resolution can be maintained even after FIB cross-sectioning of targeted HeLa cells and coupled with classification of molecular signals based on their localization inside the targeted cells. The sequence of FIB-milling coupled with SIMS imaging can be iterated, thus laying the foundation for a powerful approach to image the chemical profile of cells in 3D at submicrometer lateral resolution. Additionally, we present image visualization methods coupled with custom multivariate analysis of ion-specific images to (1) provide objective, statistically relevant image classes and (1) reveal potential subcellular localizations of biochemical interest.

Because of the complexity of ionic species desorbed from within and around single cells, as well as the difficulty in maintaining the chemical integrity of the cellular targets, care must be taken to have the proper sample preparation, sample analysis conditions that represent the optimum trade-off of spatial resolution and mass resolution, multimodal techniques such as FIB for precise sectioning of targeted cells for MS analysis, and innovation for differentiating and processing the large amounts of image data in objective and statistically relevant ways. We feel that all of these issues have been addressed in this work and that the comprehensive methodology presented herein lays the foundation for future imaging of biochemical events and cellular processes within and around single cells at submicrometer lateral resolution. Additionally, these developments can be combined with new SIMS

instruments that employ tandem mass spectrometry (MS/MS) modalities for chemical speciation of unknown mass peaks and dynamic SIMS beam currents for enhanced molecule detection, providing a potential comprehensive mass spectrometric cellular imaging paradigm.

Acknowledgments

This work was supported by the Chemical Science and Technology Laboratory (CSTL) at NIST, Gaithersburg, MD, and by the intramural program of the National Cancer Institute, NIH, Bethesda, MD. This research was performed while Jonathan Lefman held a National Research Council Research Associateship Award at NIST and NIH. The authors thank Dr. Keana Scott from NIST for her assistance in FIB milling and her valuable insights into the single cell imaging project, Dr. Andrew Konicek from NIST for additional algorithm development and manuscript editing, and Donald Bliss from the National Library of Medicine, NIH for creation of Figure 1f, which was also used as the table of content and abstract graphics.

References

This article references 48 other publications.

1. Chandra S, Bernius MT, Morrison GH. Anal. Chem. 1986; 58:493–496. [PubMed: 3963401]
2. Ausserer WA, Ling Y-C, Chandra S, Morrison GH. Anal. Chem. 1989; 61:2690–2695. [PubMed: 2619055]
3. Colliver TL, Brummel CL, Pacholski ML, Swanek FD, Ewing AG, Winograd N. Anal. Chem. 1997; 69:2225–2231. [PubMed: 9212701]
4. Lorey DR II, Morrison GH, Chandra S. Anal. Chem. 2001; 73:3947–3953. [PubMed: 11534721]
5. Fartmann M, Dambach S, Kriegeskotte C, Wiesmann HP, Wittig A, Sauerwein W, Lipinsky D, Arlinghaus HF. Surf. Interface Anal. 2002; 34:63–66.
6. Wittig A, Wiemann M, Fartmann M, Kriegeskotte C, Arlinghaus HF, Zierold K, Sauerwein W. Micros. Res. Tech. 2005; 66:248–258.
7. Lechene CP, Luyten Y, McMahon G, Distel DL. Science. 2007; 317:1563–1566. [PubMed: 17872448]
8. Chandra S, Tjarks W, Lorey DR II, Barth RF. J. Micros. 2008; 229:92–103.
9. Musat N, Halm H, Winterholler B, Hoppe P, Peduzzi S, Hillion F, Horreard F, Amann R, Jorgensen BB, Kuypers MM. M. Proc. Natl. Acad. Sci. U.S.A. 2008; 105:17861–17866.
10. Darling KF, Thomas E, Kasemann SA, Seears HA, Smart CW, Wade CM. Proc. Natl. Acad. Sci. U.S.A. 2009; 106:12629–12633. [PubMed: 19574452]
11. Eybe T, Bohn T, Audinot JN, Udelhoven T, Cauchie HM, Migeon HN, Hoffmann L. Chemosphere. 2009; 76:134–140. [PubMed: 19278714]
12. Finzi-Hart JA, Pett-Ridge J, Weber PK, Popa R, Fallon SJ, Gunderson T, Hutcheon ID, Nealson KH, Capone DG. Proc. Natl. Acad. Sci. U.S.A. 2009; 106:6345–6350. [PubMed: 19332780]
13. Slaveykova VI, Guignard C, Eybe T, Migeon HN, Hoffmann L. Anal. Bioanal. Chem. 2009; 393:583–589. [PubMed: 18985325]
14. Weber PK, Graham GA, Teslich NE, Moberly Chan W, Ghosal S, Leighton TJ, Wheeler KE. J. Micros. 2009; 238:189–199.
15. Lau KH, Christlieb M, Schroder M, Sheldon H, Harris AL, Grovenor CR. M. J. Micros. 2010; 240:21–31.
16. Fletcher JS, Vickerman JC. Anal. Bioanal. Chem. 2010; 396:85–104. [PubMed: 19669735]
17. Sjovall P, Lausmaa J, Nygren H, Carlsson L, Malmberg P. Anal. Chem. 2003; 75:3429–3434. [PubMed: 14570193]
18. Xu J, Ostrowski S, Szakal C, Ewing AG, Winograd N. Appl. Surf. Sci. 2004:231–232. 159–163.
19. Ostrowski S, Van Bell CT, Winograd N, Ewing AG. Science. 2004; 305:71–73. [PubMed: 15232100]
20. Nygren H, Malmberg PJ. Micros. 2004; 215:156–161.

21. Winograd N. Anal. Chem. 2005; 77:143A–149A.
22. Monroe EB, Jurchen JC, Lee J, Rubakhin SS, Sweedler JV. J. Am. Chem. Soc. 2005; 127:12152–12153. [PubMed: 16131155]
23. Altelaar AFM, Klinkert I, Jalink K, de Lange RPJ, Adan RAH, Heeren RMA, Piersma SR. Anal. Chem. 2006; 78:734–742. [PubMed: 16448046]
24. Fletcher JS, Lockyer NP, Vaidyanathan S, Vickerman JC. Anal. Chem. 2007; 79:2199–2206. [PubMed: 17302385]
25. Ostrowski S, Kurczy ME, Roddy TP, Winograd N, Ewing AG. Anal. Chem. 2007; 79:3554–3560. [PubMed: 17428032]
26. Parry SA, Kurczy ME, Fan X, Halleck MS, Schlegel RA, Winograd N. Appl. Surf. Sci. 2008; 255:929–933. [PubMed: 20428458]
27. Nygren H, Malmberg P, Nilsson M, Kriegeskotte C, Arlinghaus HF. Appl. Surf. Sci. 2008; 255:1285–1288.
28. Piehowski PD, Kurczy ME, Willingham D, Parry S, Heien ML, Winograd N, Ewing AG. Langmuir. 2008; 24:7906–7911. [PubMed: 18570446]
29. Piehowski PD, Davey AM, Kurczy ME, Sheets ED, Winograd N, Ewing AG, Heien ML. Anal. Chem. 2009; 81:5593–5602. [PubMed: 19530687]
30. Gunnarsson A, Kollmer F, Sohn S, Hook F, Sjovall P. Anal. Chem. 2010; 82:2426–2433. [PubMed: 20163177]
31. Kurczy ME, Piehowski PD, Willingham D, Molyneaux KA, Heien ML, Winograd N, Ewing AG. J. Am. Soc. Mass Spectrom. 2010; 21:833–836. [PubMed: 20219392]
32. Saleem M, Galla H-J. Biochim. Biohphys. Acta. 2010; 1798:730–740.
33. Roddy TP, Cannon DM Jr, Ostrowski SG, Winograd N, Ewing AG. Anal. Chem. 2002; 74:4020–4026. [PubMed: 12199569]
34. Parry S, Winograd N. Anal. Chem. 2005; 77:7950–7957. [PubMed: 16351142]
35. Nygren H, Hagenhoff B, Malmberg P, Nilsson M, Richter K. Micros. Res. Tech. 2007; 70:969–974.
36. Piehowski PD, Carado AJ, Kurczy ME, Ostrowski SG, Heien ML, Winograd N, Ewing AG. Anal. Chem. 2008; 80:8662–8667. [PubMed: 18925746]
37. Fletcher JS, Rabbani S, Henderson A, Blenkinsopp P, Thompson SP, Lockyer NP, Vickerman JC. Anal. Chem. 2008; 80:9058–9064. [PubMed: 19551933]
38. Malm J, Giannaras D, Riehle MO, Gadegaard N, Sjovall P. Anal. Chem. 2009; 81:7197–7205. [PubMed: 19639962]
39. Newbury DE, Bright DS. Microsc. Microanal. 1999; 5:333–343. [PubMed: 10473678]
40. Lehmann MJ, Sherer NM, Marks CB, Pypaert M, Mothes WJ. Cell Biol. 2005; 170:317–325.
41. Mattila PK, Lappalainen P. Nat. Rev. Mol. Cell Biol. 2008; 9:446–454. [PubMed: 18464790]
42. Szakal C, Hues SM, Bennett J, Gillen GJ. Phys. Chem. C. 2010; 114:5338–5343.
43. Brison J, Muramoto S, Castner DG. J. Phys. Chem. C. 2010; 114:5565–5573.
44. Mao D, Wucher A, Winograd N. Anal. Chem. 2010; 82:57–60. [PubMed: 19968247]
45. Winograd N, Garrison BJ. Annu. Rev. Phys. Chem. 2010; 61:305–322. [PubMed: 20055679]
46. Piwowar AM, Fletcher JS, Kordys J, Lockyer NP, Winograd N, Vickerman JC. Anal. Chem. 2010; 82:8291–8299. [PubMed: 20836508]
47. Szakal C, Kozole J, Russo MF, Garrison BJ, Winograd N. Phys. Rev. Lett. 2006; 96:216104. [PubMed: 16803256]
48. Ishitani T, Umemura K, Ohnishi T, Yaguchi T, Kamino TJ. Electron Microsc. 2007; 53:443–449.

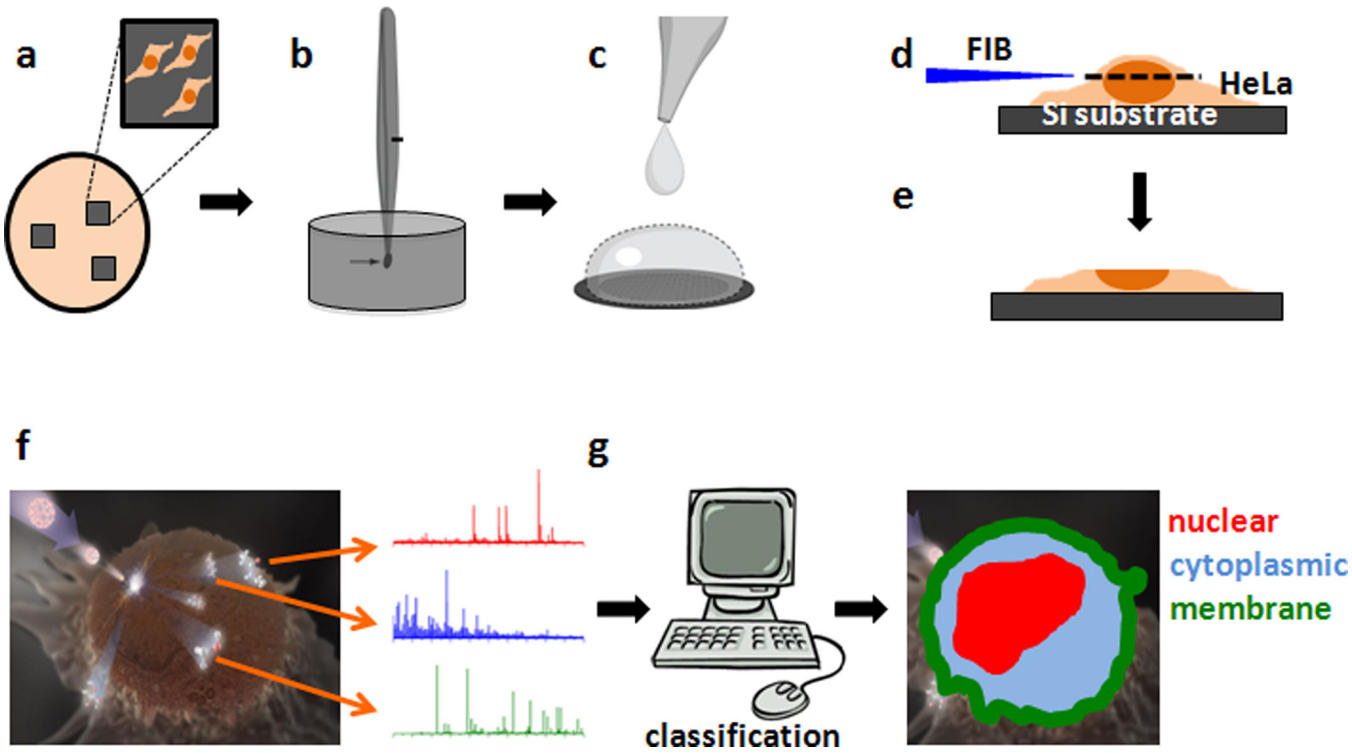

Figure 1.

Strategy for nanoscale compositional mapping of biological molecules in mammalian cells. HeLa cells are (a) grown on silicon substrates immersed in media, (b) plunge-frozen in liquid ethane, and (c) freeze-dried and gently rinsed with mass spectrometry-grade water. A tangentially directed focused ion beam (FIB) is (d) used to mill the top of the cells, which (e) exposes the cell interior. (f) Secondary ion mass spectrometry (SIMS) induced by primary ion probes such as Bi_3^+, SF_5^+, and C_{60}^+ provides hyperspectral information with submicrometer resolution on macromolecules, metabolites, and drugs in the cell interior. (g) The pixel-specific mass spectra are fed into a classification algorithm, and the extracted classes are summed and mapped as a multicolor image. Here, three sample classes corresponding to ions mapping to the nucleus (red), cytoplasm (blue), and membrane (green) are shown.

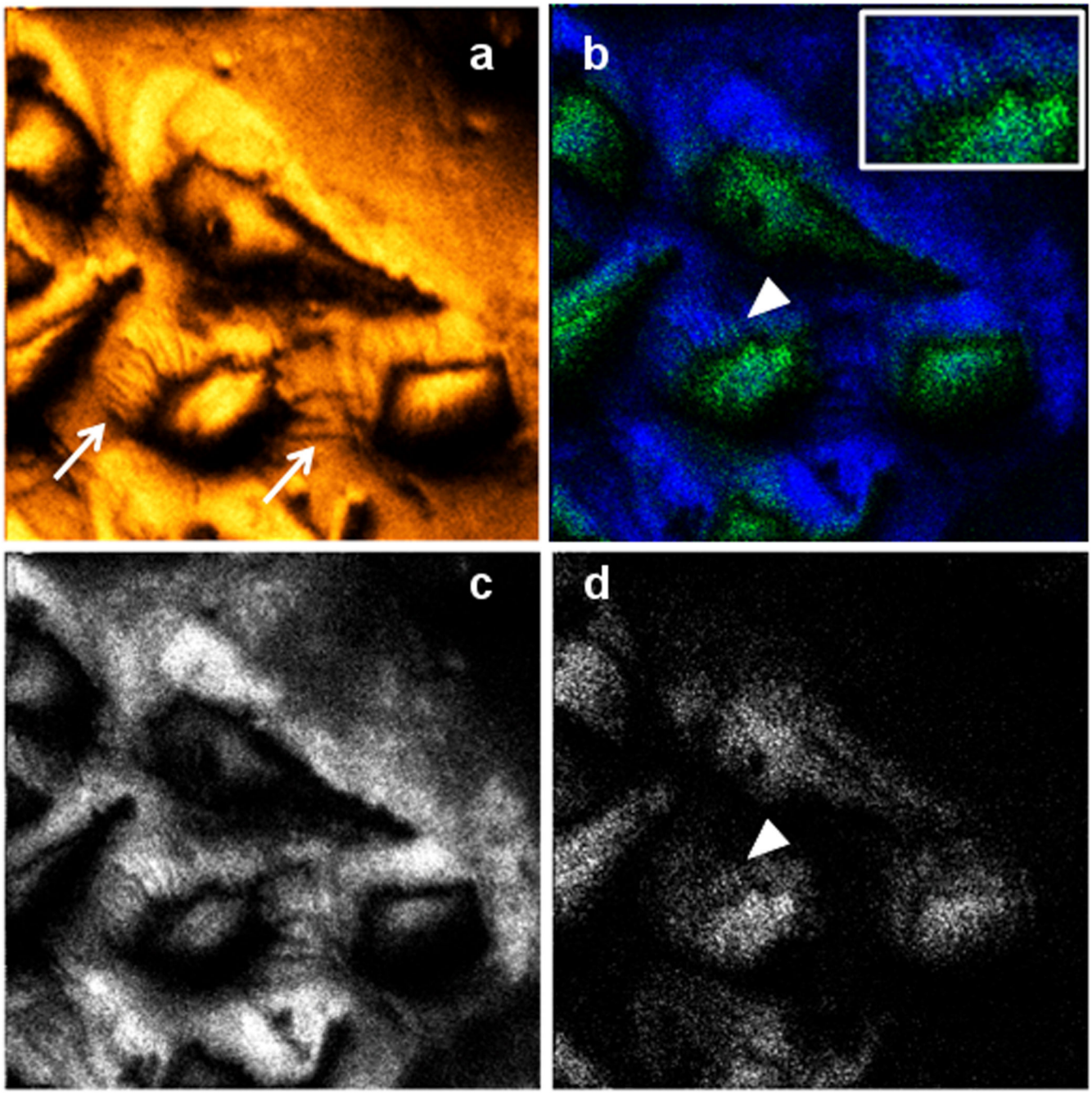

Figure 2.

Compositional mapping of HeLa cell outer lipid membranes at submicrometer resolution. (a) The total ion image (sum of all detected mass spectral components) of the surface of multiple HeLa cells. (b) A two-color image overlay of the phosphatidylcholine headgroup (*m/z* 184) in green and extracellular sodium (*m/z* 23) in blue. Parts c and d consist of individual ion-specific images for the sodium and phosphatidylcholine, respectively. The images demonstrate resolving power of approximately 400 nm by imaging the width of filopodia, identified with arrows in parts a, b, and d and shown in greater detail in the image

inset. Each image field-of-view is approximately 105 μm × 105 μm, making each pixel approximately 410 nm.

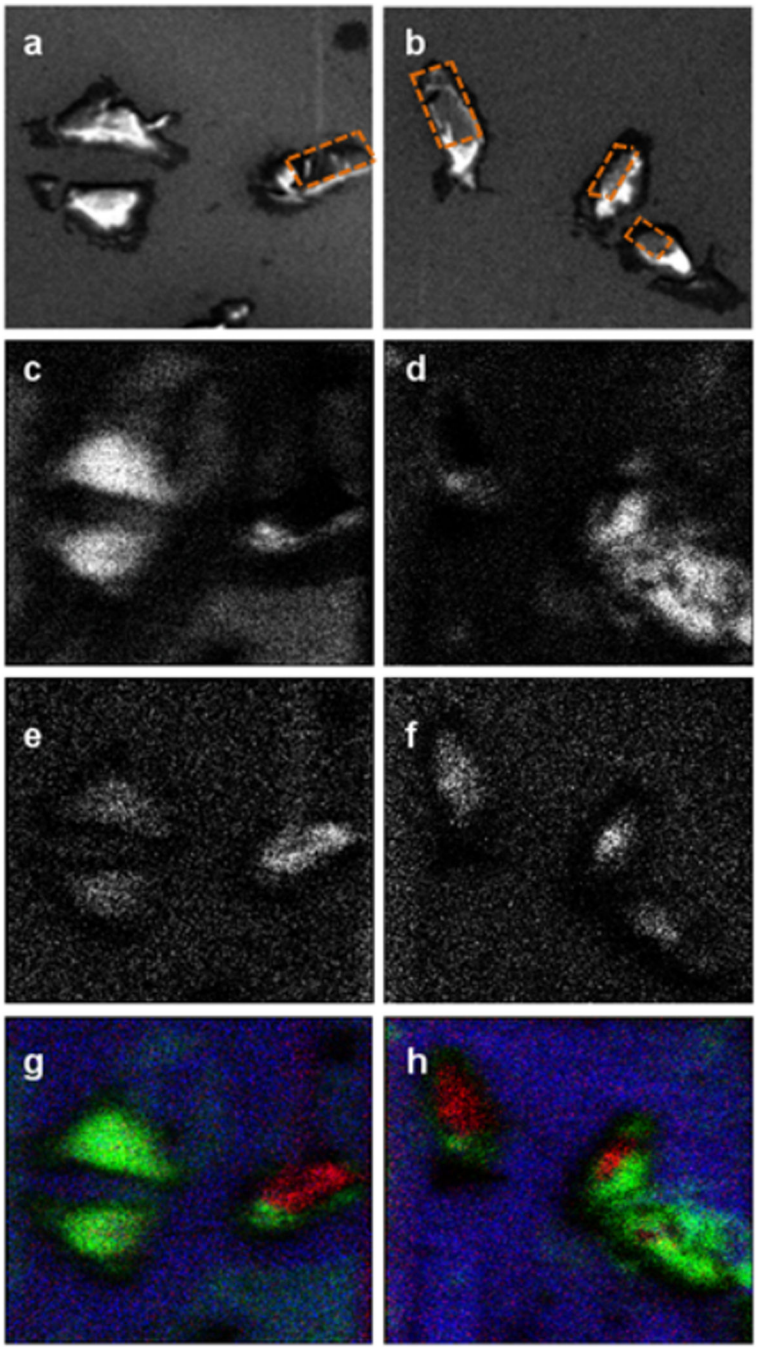

Figure 3.

Intracellular compositional maps of focused ion beam-sectioned HeLa cells by manual classification. Two separate sets of HeLa cells were milled by the focused ion beam. In one set (left panels), only one of the cells was milled [as indicated by dotted orange lines in part a], leaving two control cells untouched. In the other set (right panels), all three cells were at least partially sectioned by a wider sweep of the focused ion beam [as indicated by dotted orange lines in part b]. Since the FIB milling is parallel with the surface to remove only the tops of the respective cells, a visible change in cell shape is not observed when viewed from

above. Both sets of HeLa cells were imaged by SEM to produce the secondary electron images in parts a and b. Panels c and d display the positive polarity ion-specific images for the phosphatidylcholine lipid membrane headgroup at *m/z* 184 for each cell set. Panels e eand f display the positive polarity ion-specific images for the unassigned *m/z* 274 signature. Panels g and h display color overlays of the phosphatidylcholine headgroup (green), the *m/z* 274 signals (red), and the silicon substrate background (blue). Each image field-of-view is approximately 128 μm × 128 μm for the left panel images and approximately 121 μm × 121 μm for the right panel images, making each pixel approximately 500 and 473 nm, respectively. The SIMS-based images have not been manipulated outside of uniform brightness and contrast adjustments for improved visualization.

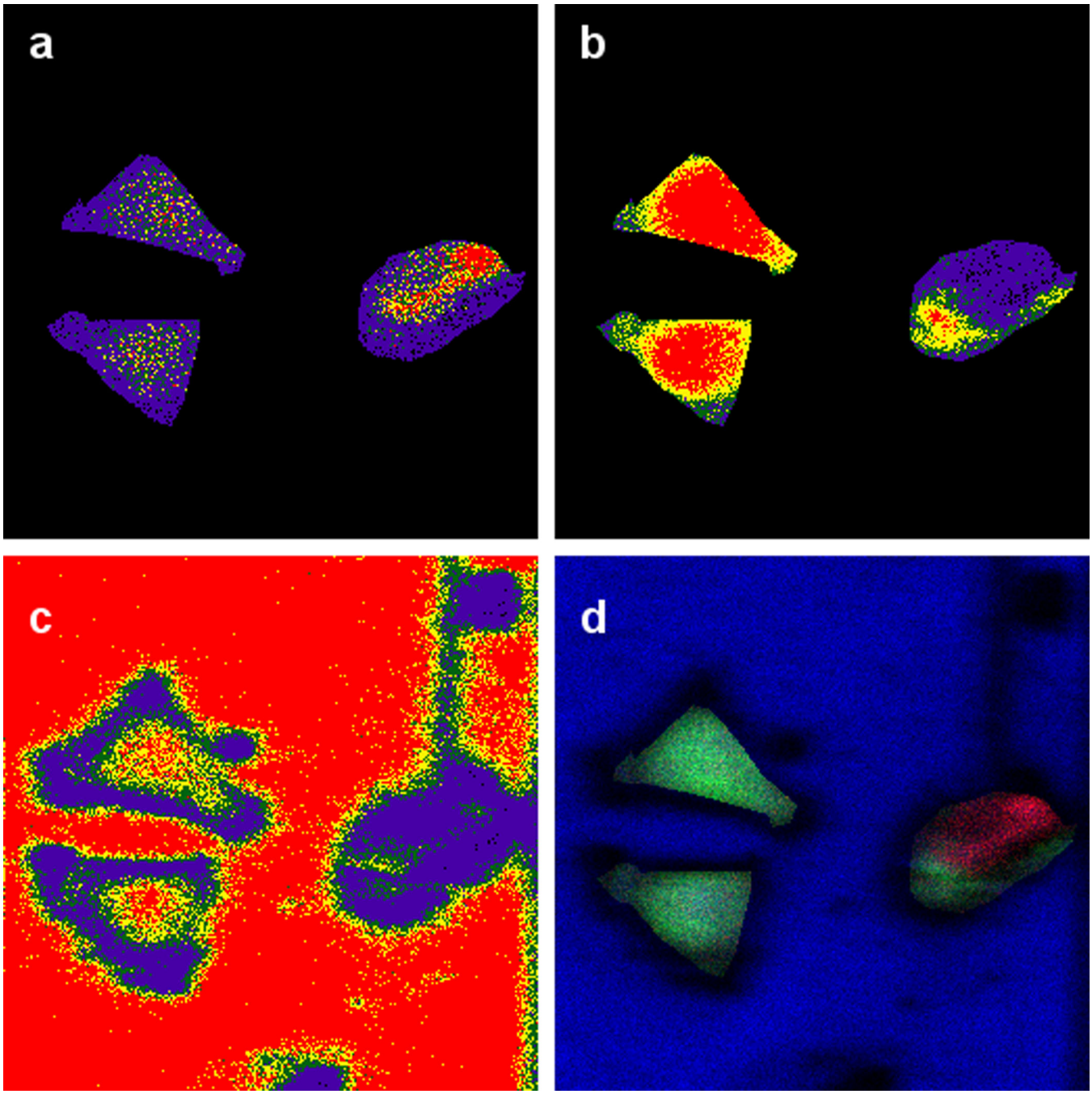

Figure 4.

Algorithm-based mapping and classification of compositional signals by their distribution within and around HeLa cells. The *k*-means-based algorithm developed herein was used to classify groups of ions having similar pixel-to-pixel image distributions after application of a cellular image mask to one of the data sets previously shown in Figure 3. All parts but part d are displayed with image pixel intensity threshold scales where pixel intensity ranges as identified below are assigned a particular color: (a) the summed image data of the three highest correlating ions within the subcellular class (*m/z* 69, *m/z* 274, and *m/z* 230); pixels of

intensity 1–49 are displayed in violet, 50–74 in green, 75–99 in yellow, and 100–255 in red. (b) Summed image data of the four highest correlating ions within the phosphatidylcholine-based class (*m/z* 104, *m/z* 58, *m/z* 86, and *m/z* 184); pixels of intensity 1–24 are displayed in violet, 25–49 in green, 50–99 in yellow, and 100–255 in red. (c) (calculated without the cellular image mask) Summed image data of the four highest correlating ions within the background class (*m/z* 30, *m/z* 44, *m/z* 70, and *m/z* 72); pixels of intensity 1–49 are displayed in violet, 50–74 in green, 75–99 in yellow, and 100–255 in red. (d) RGB three-color overlay of the three distinct classes as determined by the algorithm, with the lipid-based class in green, the subcellular class in red, and the extracellular background-based class in blue. All images are approximately 128 μm × 128 μm, making each pixel approximately 500 nm.